ACS APPLIED NANO MATERIALS

www.acsanm.org Article

Coupling between Surface Plasmon Modes of Single-Layer Complex Silver Nanohole Arrays and Enhancing Index Sensing

Yanfeng Wang, Shen Ao, Fei Yang, Zhengjun Zhang,* and Yiping Zhao*

Cite This: https://doi.org/10.1021/acsanm.2c01962 Read Online

ABSTRACT: By independently tuning the structure parameters of the nanorods in nanohole arrays (NRinNH), the localized surface plasmon resonance (LSPR)-induced extraordinary optical transmission (EOT) mode and the surface plasmon polariton (SPP)-induced EOT modes can be coupled to introduce a mode splitting phenomenon in a simple one-layer plasmonic nanostructure. We demonstrate that the coupling and energy exchange of the two different types of EOT modes of the NRinNH structure can simultaneously improve the near-field electromagnetic enhancement and spectral resolution of the LSPR-induced EOT peak, while they reduce the spectral resolution of the SPP-induced EOT modes. The hybrid modes of the NRinNH structure can be tuned to the NIR wavelength region by the length of the NR, of which the large resonance wavelength is highly preferred for improving the refractive index sensitivity (RIS) of the plasmonic sensor. In addition, using the difference in the polarization transmission spectra of NRinNH structures, the figure of merit (FOM) of the sensor performance can be significantly improved. The effect of coupling on different EOT modes in plasmonic sensing is systematically studied. A high RIS of 1200.6 nm/RIU and a high FOM of 279.2 RIU^{-1} are achieved. This provides guidance for the design of LSPR sensors based on complex NH structures with high FOM.

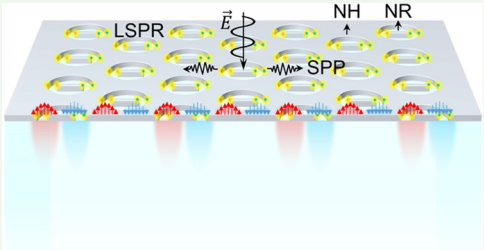

KEYWORDS: *one-layer plasmonic nanostructure, nanorod in nanohole, extraordinary optical transmission, coupled oscillator model, plasmonic sensor, figure of merit*

1. INTRODUCTION

Localized surface plasmon resonances (LSPRs) confine light on the nanometer scale and can strongly promote the light–matter interactions. The most significant properties of LSPRs are their local electromagnetic field enhancement effect and fast damping mechanism (wide spectral width).[1] The local-field enhancement prompts LSPR-enhanced nonlinear optical processes, Purcell enhancement, photoharvesting, etc. However, the fast damping of LSPRs leads to a large spectral width and short dephasing time of the coherent resonance, which can potentially limit some LSPR-based applications. For example, plasmonic sensors, based on the response of LSPR to the changes in the surrounding dielectric environment, require high refractive index sensitivity (RIS) and high spectral resolution.[2] The RIS of a wavelength interrogated sensor is defined in terms of the change in peak position ($\Delta\lambda$) per "refractive index (n) unit" (RIU), RIS = $\Delta\lambda/\Delta n$. The spectral resolution is mainly determined by the linewidth and the intensity of the spectral peak, typically represented by the full width at half-maximum (FWHM). A sharp and intense sensing peak facilitates the ease of the recognition of a peak shift and increases the analysis accuracy, which can be characterized by a parameter called the figure of merit (FOM), FOM = RIS/FWHM. For LSPRs, the wide spectral width limits the improvement of the FOM of plasmonic sensors. The applications for LSPR-based fluorescence enhancement also favor longer dephasing times, i.e., sharper spectral width.

Manipulating the spectral width of LSPR is highly desirable. One way to decrease the spectral width is the excitation of subradiant modes attributed to the reduction of the radiation loss.[3] However, these modes are typically dark, that is, they cannot easily be excited by incident light.[4] The interaction between the localized plasmons associated with the nanoparticles and light diffracted by the array (diffractively coupled LSPR) can significantly improve the quality of LSPR.[4,5] However, the right combination of nanoparticle size and shape, together with an appropriate array period, is required for the light scattered by each nanoparticle into the plane of the array to be in phase with the plasmon resonance induced in its neighbor. In addition, a homogeneous refractive index environment is necessary to observe this diffractively coupled LSPR at normal incidence for arrays of relatively thin nanostructures,[4,6] which will limit its application in real sensing. These pathways toward manipulating the spectral

Received: May 5, 2022
Accepted: May 31, 2022

width rely on a substantial increase in the complexity of the design and arrangement of the plasmonic nanostructures. Alternatively, the coupling between different plasmon modes and/or other resonance modes can result in new hybrid modes, the spectral width of which can also be manipulated due to exchanging mutual information between the uncoupled modes.[1] Yang et al. experimentally manipulated the spectral width of coupled plasmon modes under strong coupling between LSPRs and propagating surface plasmon polaritons (SPPs) utilizing a metal−insulator−metal (MIM) (Au thin film/Al_2O_3 spacer/Au nanodisk array) structure.[1] Chanda et al. reported methods to enhance and modify the plasmonic resonances in cavity-coupled quasi-three-dimensional (3D) plasmonic crystals by coupling them strongly to optical modes of Fabry−Perot-type cavities.[7] However, most of the plasmonic nanostructures used in the study of mode coupling require multilayers, in which different layers support different resonance modes.[8−11] In general, a top layer with a periodic metallic nanostructure array supporting the LSPR and/or SPP is necessary. For other layers, different materials and structures can be used, depending on the mode selection, i.e., a semiconductor layer for the waveguide modes[12] and a thick dielectric spacer with a metallic thin reflector for cavity modes.[7,11] The complex multilayer nanostructures will cause a substantial increase in the difficulty and cost of fabrication. It is very challenging to develop a simple and single-layered plasmonic nanostructure but also has high field enhancement and high spectral resolution.

Periodic subwavelength nanoholes (NH) combined with other metallic nanostructures can realize both the LSPR and SPP modes simultaneously through a simple one-layer plasmonic nanostructure.[13,14] In addition, the two different modes can be tuned separately by adjusting the structural parameters and the coupling of the two different modes can be simply and directly observed through the transmission spectrum. The SPPs on the NH array can result in multiple optical resonance peaks, which display a higher transmission intensity compared to the incident light when normalized to the perforated area ratio, i.e., the extraordinary optical transmission (EOT).[15,16] These SPP-induced EOT peaks possess a narrow and asymmetric spectral shape, red shift linearly with the periodicity of the perforated NH structures, and show a strong response to changes in the refractive index (RI) of the material around the two sides of the film. While, for the compound NH structures, in particular, the nanorod in nanohole (NRinNH) structures, a new EOT peak caused by the coupling of LSPR of NR and NH appears and red shifts exponentially with the NR length.[13,14] The NRinNH structures have been systematically studied theoretically[13,14] and experimentally have been realized via multistep nanosphere lithography (NSL).[17,18] Since the SPP-induced EOT peaks red shift linearly with the periodicity of the compound structure while the LSPR-induced EOT peak depends on the size of NR and NH, the LSPR- and SPP-induced EOT peaks can be tuned independently by varying different structural parameters. Thus, it is possible to introduce coupling of the two different types of EOT modes by varying different structural parameters, such as the NR length and the width, the location of NR, the hole diameter, and the periodicity of the structure. The obvious EOT peaks in the transmission spectrum can facilitate the observation of the coupling phenomenon. The coupling of two different EOT modes could potentially achieve a narrow spectral peak with a high RIS and an appropriate resonance wavelength. In addition, the polarization-dependent spectra caused by structural anisotropy, parallel and vertical to the long axis of the NR, can help to improve the FOM of index refractive sensing by tracking the zero-crossing points (ZCPs) of the difference between the two polarized spectra.[2]

In this work, a simple one-layer NRinNH plasmonic nanostructure with hybrid modes of the LSPR and SPP is designed. We demonstrate that by varying the periodicity of the NH array and the length of NR, the coupling and energy exchange of SPP and LSPR modes of the NRinNH structure can simultaneously improve the near-field electromagnetic enhancement and spectral resolution of the LSPR-induced EOT peak, though the spectral resolution of the SPP-induced EOT mode is declined. In addition, the coupling region can be tuned to the NIR wavelength region by the length of the NR, thus the EOT peaks of hybrid modes can be realized in the NIR region or even larger wavelength. The large resonance wavelength is beneficial for high-sensitivity plasmonic sensors because there is a definite relationship between RIS and the resonance wavelength λ_0, i.e., as λ_0 increases, the RIS increases.[19] The effect of coupling on different EOT modes in plasmonic sensing is systematically studied, and the improvement and deterioration of the sensing performance of LSPR- and SPP-induced EOT modes, respectively, are demonstrated. The difference in the polarized transmission spectra of NRinNH structures is used to further improve the FOM of the sensor performance. As an example of the sensing application, a high RIS of 1200.6 nm RIU^{-1} and a high FOM of 279.2 RIU^{-1} are demonstrated for index refractive sensing.

2. RESULTS AND DISCUSSION

2.1. Coupling Phenomenon in the Transmission Spectra. The NRinNH structure is a hexagonal array with a period of L, as shown in Figure 1. The NR is in the center of the NH. The layer thickness (h), hole diameter (D), NR length (l), and width (w) were fixed at 50, 340, 200, and 30 nm, respectively, unless otherwise specified. A commercial finite-difference-time-domain (FDTD) software system (Ansys Lumerical 2021 R1 Finite Difference IDE) was used to calculate the transmission spectra $T(\lambda, \varphi)$ and localized E_z-field distributions of the NRinNH structures. The polarization angle φ is the angle between the polarization direction of the incident light and the long axis of NRs. Detailed FDTD calculation conditions can be referred to in Section S1 of the Supporting information (SI).

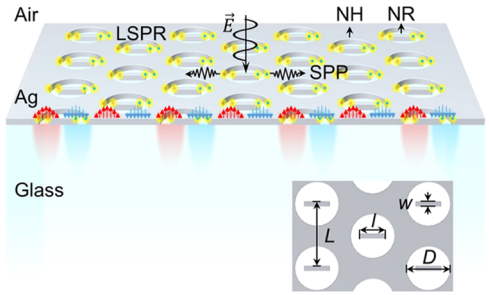

Figure 1. Schematic diagram for the nanostructure and the hybrid mode. The LSPR mode is located mainly at the ends of the NRs. The SPP-Bloch wave is confined mainly at the Ag−air or Ag−glass interface. The schematic shows only the hybrid mode at the Ag−air interface. The colored arrows are a simple representation of the E_z component of the local electric field.

https://doi.org/10.1021/acsanm.2c01962
ACS Appl. Nano Mater. XXXX, XXX, XXX−XXX

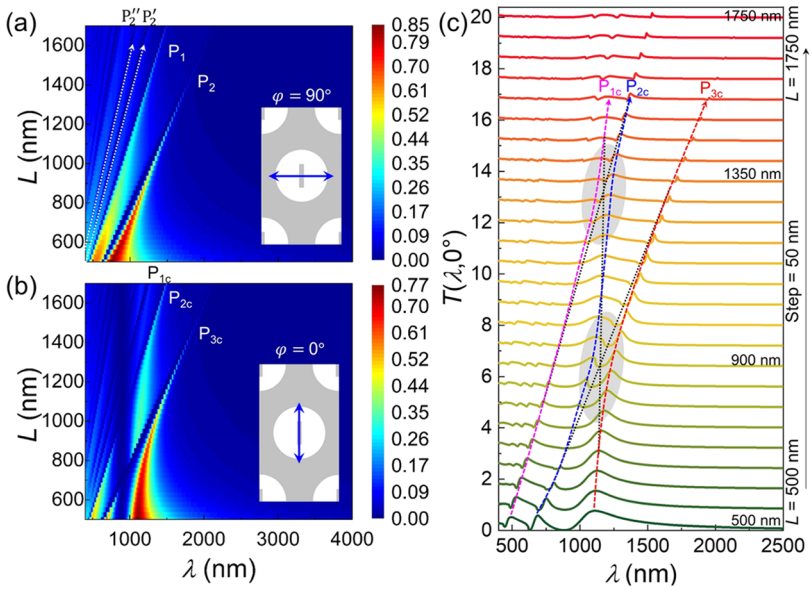

Figure 2. (a) $T(\lambda, 90°)$ spectra of the NRinNH structures with different *L*s. The inset figure shows the polarization direction of the incident light ($\varphi = 90°$). (b) $T(\lambda, 0°)$ spectra of the NRinNH structures with different *L*s. The inset figure shows the polarization direction of the incident light ($\varphi = 0°$). (c) Typical $T(\lambda, 0°)$ spectra of the NRinNH structures with different *L*s. The dotted lines correspond to the uncoupled SPP- and LSPR-induced EOT modes. The dashed arrows represent the coupled modes.

The calculated $T(\lambda, \varphi)$ of NRinNH with different *L*s (0.5−1.7 μm) and fixed nanostructure size is presented in Figure 2a,b for φ = 90 and 0°, respectively. When φ = 90°, the longitudinal LSPR mode of NR is not excited and $T(\lambda, 90°)$ is very similar to that of the corresponding NH array (Figure S1) with the same lattice arrangement and dimensions. As *L* increases, the two main EOT peaks (P_1 and P_2) red shift linearly, and their resonance wavelengths λ_{P_1} and λ_{P_2} versus *L* almost overlay with that of the corresponding NH array (Figure S1). This demonstrates that the two main peaks in $T(\lambda, 90°)$ of the NRinNH structures have the same physical origins as those of the corresponding NH array. In principle, the EOT resonance peaks for a pure hexagonal NH array should occur at wavelengths corresponding to the grating matching condition required for the excitation of SPPs on the metal/dielectric interfaces[20,21]

$$\lambda_{SPP}(i, j) = \frac{\sqrt{3}L}{2\sqrt{i^2 + ij + j^2}}\sqrt{\frac{\varepsilon_{Ag}\varepsilon_d}{\varepsilon_{Ag} + \varepsilon_d}} \quad (1)$$

where (*i*, *j*) are the grating orders of the peaks, ε_{Ag} is the relative permittivity of Ag (real component), and ε_d is the relative permittivity of the dielectric material in contact with the upper (air) and lower (glass) NH interfaces. In practice, a transmission minimum, instead of a transmission maximum, is routinely observed at this particular resonance wavelength.[22] This counterintuitive observation is associated with the fact that the grating matching condition defined above is for SPP's propagation on a perfectly uniform and continuous Ag layer. Enhanced light transmission requires the coupling of SPPs to the LSPs at the rims of the NHs.[22−24] However, both the transmission minima before P_1, P_2, and the peaks P_1 and P_2 red shift linearly with *L* when the size of NR and NH are fixed. P_1 and P_2 represent the EOT peaks induced by the (0, 1) SPP modes at the Ag−air and Ag−glass interfaces, respectively. P_2' and P_2'' marked in Figure 2a represent the EOT peaks induced by the higher-order SPP modes at the Ag−glass interface ((1, 1) and (0, 2), respectively).

When φ = 0°, the longitudinal LSPR mode of NR is excited and a peak P_3 due to the local electromagnetic coupling of NH and NR emerges.[14] Based on the systematic study in refs 13, 14, the resonance wavelength of P_3 depends only on the length of NR and the size of NH as well as their relative positions. As proof, the $T(\lambda, 0°)$ of NRinNH of longer NR (330 nm) and different *L*s is shown in Figure S2. The resonance wavelength λ_{P_3} of P_3 at around 2.4 μm remains unchanged when *L* increases from 500 to 1400 nm. Since both λ_{P_1} and λ_{P_2} increase linearly with *L*, while λ_{P_3} is a constant for a fixed *l* and *D*, it is expected that at a particular L_c value, $\lambda_{P_2} = \lambda_{P_3}$ or $\lambda_{P_1} = \lambda_{P_3}$. Based on Figure 2b, for *l* = 200 nm and *D* = 340 nm, L_c is expected to be around 900 and 1350 nm, respectively. Therefore, it is expected that in the vicinity of L_c, both the SPP-induced and the LSPR-induced EOT resonances overlap, and the local field generated at the SPP-induced EOT modes shall couple with the local field generated at the LSPR-induced EOT mode. The evanescent electromagnetic field of the SPP-induced EOT modes (P_1 or P_2) exhibits interaction with the LSPR-induced EOT mode of the compound nanostructures (P_3) and results in spectral doublets that display avoided crossings, as shown in the progression of the spectra with increasing *L* in Figure 2b.[12] To show the avoided crossings clearly, Figure 2c plots some typical $T(\lambda, 0°)$ spectra of the NRinNH structures with fixed structural parameters but different *L*s; the gray shaded areas show the coupling regions. The dotted lines in Figure 2c correspond to the uncoupled SPP- and LSPR-induced EOT modes. The dashed arrows represent the coupled modes. We use P_{1c}, P_{2c}, and P_{3c} to represent the EOT peaks for the NRinNH structures with the coupling phenomenon, as shown in Figure 2b and 2c. The pink dashed arrow in Figure 2c represents the EOT mode P_{1c}, the blue dashed arrow represents the EOT mode P_{2c}, and the red dashed arrow represents the EOT mode P_{3c}. Two clear

https://doi.org/10.1021/acsanm.2c01962
ACS Appl. Nano Mater. XXXX, XXX, XXX−XXX

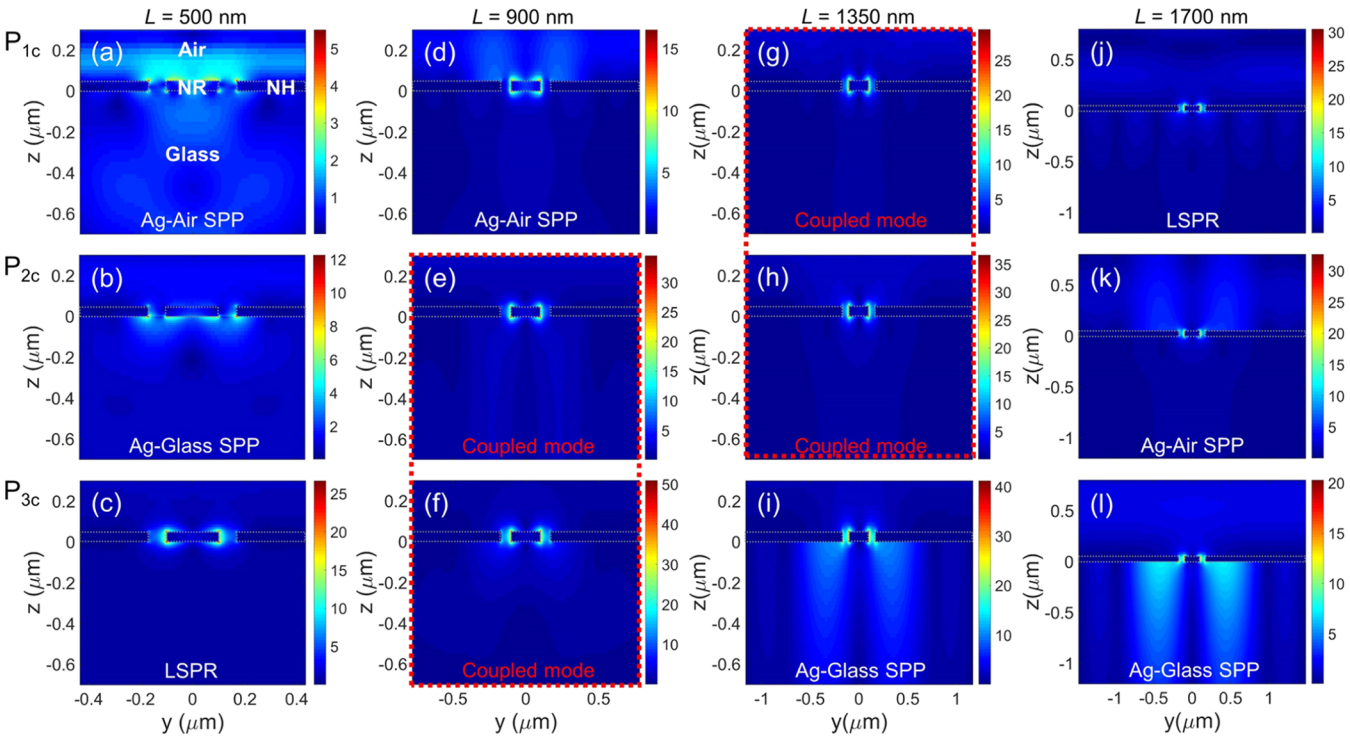

Figure 3. Normalized electric field $|E/E_0|$ distributions at $\lambda_{P_{1c}}$, $\lambda_{P_{2c}}$, and $\lambda_{P_{3c}}$ for NRinNH structures with (a−c) L = 500 nm, (d−f) L = 750 nm, (g−i) L = 1350 nm, and (j−l) L = 1700 nm, respectively.

anticrossings (at L ∼900 and ∼1350 nm) of the dashed arrows in the transmission spectra can be seen. The spectra feature changes a lot in the coupling region when compared to the spectra of smaller L in the uncoupled region. A clear asymmetric Fano line shape of the coupled EOT modes can be observed due to the interaction of a narrow line-shape resonance (SPP-induced EOT mode) with a broad resonance (LSPR-induced EOT mode). The LSPR mode usually possesses a wider spectral width because of the larger dissipation when compared to the SPP mode.[1] The anticrossings are also confirmed by the electric field spectra in the near-field, as shown in Figures S3 and S4. The $T(\lambda, 0°)$ of NRinNH of fixed L (1350 nm) and different ls (from 50 to 330 nm) is also calculated and shown in Figure S5. When l < 120 nm, no coupling is observed, while, when l is in a 125−330 nm length region, anticrossings similar to those in Figure 2b can be observed.

2.2. Energy Exchange in the Process of Mode Coupling. To understand the energy exchange between the LSPR plasmon- and SPP-Bloch wave character of the polaritons at the coupling region, we use FDTD to calculate the normalized electric field intensity $|E/E_0|$ maps at $\lambda_{P_{1c}}$, $\lambda_{P_{2c}}$, and $\lambda_{P_{3c}}$ to find out the mode distributions. E_0 is the electric field amplitude of the incident wave at the corresponding wavelength. At a small period (L = 500 nm), three separated peaks appear on the transmission spectrum, as shown in Figure 2c. Peaks P_{1c} and P_{2c} have a narrow spectral width, and the electric field is confined mainly on the surfaces of the Ag film (the Ag−air interface in Figure 3a and the Ag−glass interface in Figure 3b). The peak P_{3c} has a broad spectral width, and the electric field is located mainly at the two ends of the NR, with a greater field enhancement, as shown in Figure 3c. Therefore, we recognize that the P_{1c} and P_{2c} represent the SPP-induced EOT mode at the two interfaces and P_{3c} is the LSPR mode at this L value.

When L is changed to 900 nm, three main peaks can still be identified in the transmission spectrum, as shown in Figure 2c. The P_{1c} peak remains sharp, while P_{2c} and P_{3c} peaks become similar, and similar electric field distributions can be acquired at $\lambda_{P_{2c}}$ and $\lambda_{P_{3c}}$, as shown in Figure 3e,f. The coexistence of LSPR and diffracted propagating waves is visible: the LSPR occurs at the ends of the NR and the diffracted field is apparently near the unperforated region at the Ag/glass interface. In this case, the SPP-induced EOT mode P_{2c} can be coupled to the LSPR-induced EOT mode P_{3c}; thus, the energy is exchanged reversibly between the two coupled modes. The energy exchange demonstrates that the coupling between the LSPR mode and the SPP mode modifies the field distribution resulting from the normal-mode splitting with the small detuning. Then, when L is changed to 1350 nm, the P_{3c} peaks become very sharp and the electric field is confined mainly to the Ag−glass interface. Therefore, we recognize that after the coupling and energy exchange of P_{2c} and P_{3c}, the P_{3c} now represents the SPP-induced EOT mode at the Ag−glass interface. The peak shape of P_{1c} and P_{2c} becomes similar at this L value, as shown in Figure 2c, and similar electric field distributions can be revealed at P_{1c} and P_{2c}, as shown in Figure 3g,h. The coexistence of LSPR and diffracted propagating waves is visible: the LSPR occurs at the ends of the NR and diffracted field is near the unperforated region at the Ag/air interface. In this case, the SPP-induced EOT mode is coupled to the LSPR mode and the energy is exchanged reversibly between the two coupled modes.

When L is changed to 1700 nm, the strongly confined electric field at the Ag−glass interface shown in Figure 3l indicates that P_{3c} still represents the SPP-induced EOT mode at the Ag−glass interface, similar to when L = 1350 nm, as

https://doi.org/10.1021/acsanm.2c01962
ACS Appl. Nano Mater. XXXX, XXX, XXX−XXX

shown in Figure 3i. The peak P_{2c} becomes very sharp (Figure 2c) and the electric field is confined mainly to the Ag−air interface, as shown in Figure 3k. The electric field of P_{1c} is located mainly at the two ends of the NR, as shown in Figure 3j. Therefore, after the energy exchange in the coupling region of P_{1c} and P_{2c}, the P_{2c} now represents the SPP-induced EOT mode at the Ag−air interface and P_{1c} represents the LSPR-induced EOT mode.

2.3. Coupled Oscillator Model (COM), Spectral Shape Change, and Enhanced Local Electric Fields. The physical origin of the coupling can be captured by a model of coupled three harmonic oscillators, which leads to the following phenomenological (non-Hermitian) Hamiltonian[1,12,25]

$$H = \begin{pmatrix} E_{P_3} - i\hbar\Gamma_{P_3} & V_2 & V_1 \\ V_2 & E_{P_2} - i\hbar\Gamma_{P_2} & \\ V_1 & & E_{P_1} - i\hbar\Gamma_{P_1} \end{pmatrix}$$

where E_{P_1}, E_{P_2}, and E_{P_3} are the resonance photon energies of the uncoupled peaks P_1, P_2, and P_3 (corresponding to three oscillators, respectively). E_{P_1} and E_{P_2} change inversely with L, while E_{P_3} is a constant, as shown in Figure 4a. Γ_{P_1}, Γ_{P_2}, and Γ_{P_3} are the corresponding damping frequencies of P_1, P_2, and P_3, respectively. The constants V_1 and V_2 are the coupling potential describing the coupling strength between the oscillators P_1 and P_3, P_2, and P_3, respectively. The V_1 and V_2 dictate the energy splitting observed at the resonance (when $E_{P_1} = E_{P_3}$ or $E_{P_2} = E_{P_3}$). The eigenvalues of the Hamiltonian represent the new eigenenergies of the coupled system, i.e., the final resulted peaks shown in Figure 2b,c. Based on the extracted P_{1c}, P_{2c}, and P_{3c} location as a function of L, the fitted coupling potentials are obtained as V_1 = 40.8 meV and V_2 = 59.2 meV. The eigenenergies resulting from this Hamiltonian with the fitted coupling constants V_1 and V_2 are given by the solid curves shown in Figure 4a, which satisfactorily reproduce the calculation data extracted from the $T(\lambda, 0°)$ spectra shown in Figure 2b (details are shown in Section S6 in SI). The slight mismatch between COM and $E_{P_{1c}}$ at L ∼1600−1800 nm is due to the influence of the coupling between higher-order SPP-induced EOT modes (P_2' and P_2'') with P_3. From the transmission spectrum shown in Figure 2a, the dissipation frequencies of P_2 and P_1 are estimated: $\hbar\Gamma_{P_2} \approx 50.2$ meV at L = 900 nm and $\hbar\Gamma_{P_2} \approx 46.0$ meV at L = 1350 nm. For the uncoupled LSPR mode, the dissipation frequency can be estimated from the transmission spectrum of NRinNH structures with a longer NR (l = 330 nm), as shown in Figure S2. $\hbar\Gamma_{P_3} \approx 50.0$ and 38.7 meV at L = 900 and 1350 nm, respectively. The results verify that the interaction of P_2 and P_3 is in the strong coupling regime because the interaction potential (59.2 meV) is larger than the average dissipation ($\sqrt{(\hbar\Gamma_{P_2})^2/2 + (\hbar\Gamma_{P_3})^2/2} = 50.1$ meV). The energies of the uncoupled SPP-induced EOT modes are denoted by the dashed-dot curve and dashed curve, and the unperturbed LSPR-induced EOT mode is denoted by the horizontal dotted line, as shown in Figure 4a. At where the dashed curves and dotted line intersect (marked by yellow (P_2 and P_3 at around L = 900 nm) and green (P_1 and P_3 at around L = 1350 nm) stripes), the positions of transmission peaks present obvious anticrossings (P_{2c} and P_{3c}, P_{1c} and P_{2c}). The splitting energies

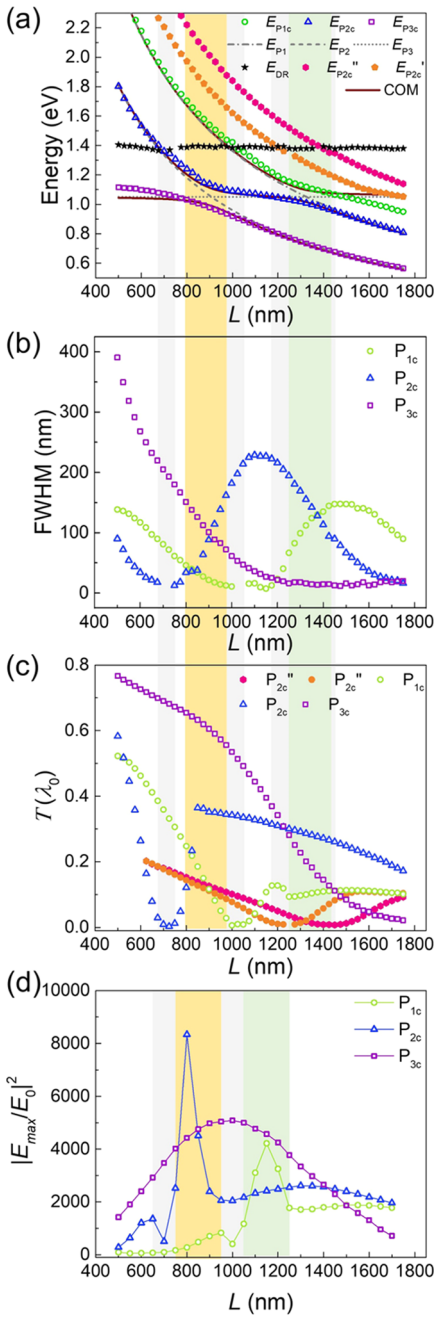

Figure 4. (a) Energy dispersion relationships of the three branches P_{1c}, P_{2c}, and P_{3c} plotted against L. The horizontal dotted line represents the energy of the uncoupled LSPR-induced EOT mode P_3 and the dashed-dot and dashed curves represent the energies of the uncoupled SPP-induced EOT modes P_1 and P_2, respectively. The solid lines correspond to the real part of the eigenenergies of the coupled modes calculated by the coupled oscillator model (COM) with a splitting energy of 160.0 meV at $E_{P_2} = E_{P_3}$ (L ∼ 900 nm) and 107.3 meV at $E_{P_1} = E_{P_3}$ (L ∼ 1350 nm). (b) Plots of the FWHM of the peaks, (c) transmittance at λ_0, and (d) volume maximum local electric field enhancement $|E_{max}/E_0|^2$ of the gap between the NR and the NH for λ_0 of NRinNH structures with different Ls.

are calculated as 160.0 meV at $E_{P_2} = E_{P_3}$ (L ∼ 900 nm) and 107.3 meV at $E_{P_1} = E_{P_3}$ (L ∼ 1350 nm). In this case of small detuning, the SPP-induced EOT modes can be coupled to the LSPR-induced EOT mode and the energy is exchanged

https://doi.org/10.1021/acsanm.2c01962
ACS Appl. Nano Mater. XXXX, XXX, XXX−XXX

reversibly between the two coupled modes. Away from the coupling regimes, the transmission peak positions approach that of the uncoupled resonances. The energy of the unperturbed LSPR-induced EOT mode is calculated to be 1050.5 meV (λ_{P_3} = 1180 nm). This model predicts the formation of three polariton states (P_{1c}, P_{2c}, and P_{3c}) at the coupling region, which are superpositions of SPP- and LSPR-induced EOT states. These states have properties that differ from those of the uncoupled subsystems, including their spectral line widths.

According to the COM, incident light energy can be reversibly exchanged between the plasmon- and SPP-Bloch wave character of the polaritons, which results in narrower spectra width for the plasmon-like excitations. To study the influence of the energy exchange between the LSPR- and SPP-induced EOT modes on spectra features, we extracted the FWHM and transmittance of the peaks for different *L*s. The volume maximum local electric field enhancement $|E_{max}/E_0|^2$ of the gap between NR and NH at the resonance wavelength of the peaks ($P_{1c} \sim P_{3c}$) is also calculated. Figure 4b plots the FWHM of the peaks of different *L*s. In general, the spectra width of the LSPR-induced EOT peaks decreases when coupling with the SPP-induced EOT peaks, while the spectra width of the SPP-induced EOT peaks increases at the coupling region. Specifically, at the coupling region of P_{2c} and P_{3c} (the yellow color stripe at $L \sim 900$ nm), the FWHM of P_{3c} (LSPR-induced EOT peak) decreases with the increase in *L*, while the FWHM of P_{2c} (SPP-induced EOT peak) increases with *L*. After the energy exchange in the coupling region of P_{2c} and P_{3c} ($L > \sim 900$ nm), P_{3c} represents the SPP-induced EOT mode at the Ag−glass interface and P_{2c} represents the LSPR mode. At the coupling region of P_{1c} and P_{2c} (the green color stripe at $L \sim 1350$ nm), the FWHM of P_{2c} (LSPR-induced EOT peak) decreases with the increase in *L*, while the FWHM of P_{1c} (SPP-induced EOT peak) increases with *L*. After the energy exchange in the coupling region of P_{1c} and P_{2c} ($L > 1350$ nm), P_{2c} represents the SPP-induced EOT mode at the Ag−air interface and P_{1c} represents the LSPR mode. Thus, the energy exchange between the LSPR- and SPP-induced EOT modes results in a narrower FWHM for the LSPR excitations, which is beneficial for high-performance sensing applications. To further confirm that the FWHM of the LSPR-induced EOT mode is narrowed at the coupling region, the plasmon phase relaxation dynamics is simulated with a time monitor, and the near-field electrical spectra of different *L*s are shown in Figure S6. The fitted dephasing times of the coupled modes, 32.9 and 18.9 fs of P_{3c} and P_{2c} at L_c = 900 nm or 18.0 and 28.7 fs of P_{2c} and P_{1c} at L_c around 1300 nm, are longer than the dephasing times of the pure LSPR modes, 12.4 fs of P_3 for $L_c < 900$ nm and 11.6 fs of P_2 for $L_c > 900$ nm or 11.6 fs of P_2 for $L_c < 1300$ nm and 16.2 fs of P_1 for $L_c > 1300$ nm, which also proves that the coupling of the LSPR-induced EOT mode with the SPP-induced EOT modes can reduce the spectra width of the LSPR mode. Details can be found in Section S7 of the SI.

Figure 4c plots $T(\lambda_0)$ of the resonant peaks of different *L*s. Overall, the transmittance of different peaks decreases with the increases in *L* due to the decrease in the perforation area ratio. However, a minimum transmittance of the peaks appears around the excitation wavelength of the longitudinal LSPR mode of NR. The black stars in Figure 4a show the resonance wavelength at around 890 nm of the longitudinal LSPR mode of NR (D_R). The strong resonant light absorption possibly causes the transmittance of all of the peaks at $\lambda_0 \approx \lambda_{D_R}$ to be very low (near zero), as indicated in Figure 4c (marked by a gray color stripe). With *L* continuing to increase, $\lambda_0 > \lambda_{D_R}$, the transmittance of the peaks recovers to a certain value and continues to decrease with the increase in *L*. Coupling seems to have little impact on the peak transmittance, as indicated by the yellow and green color stripes.

The volume maximum local electric field enhancement $|E_{max}/E_0|^2$ and the average local electric field enhancement $|E_{mean}/E_0|^2$ of the gap between NR and NH at λ_0 are calculated and shown in Figures 4d and S7 in the SI. $|E_{mean}/E_0|^2$ and $|E_{max}/E_0|^2$ of the gap between NR and NH at $\lambda_{P_{1c}}$ and $\lambda_{P_{2c}}$ show a similar trend versus *L*: with the increase in *L*, both $\lambda_{P_{1c}}$ and $\lambda_{P_{2c}}$ red shift and become closer to the resonance wavelength of D_R (gray stripe), the field enhancement decreases. A further increase in *L* causes both $\lambda_{P_{1c}}$ and $\lambda_{P_{2c}}$ to red shift and be closer to the resonance wavelength of the uncoupled LSPR-induced EOT mode λ_{P_3}. The coupling between P_{2c} with P_{3c} (yellow stripe) and P_{1c} with P_{2c} (green stripe) causes the field enhancement to continuously increase. At a certain *L* value (∼800 and 1175 nm), the field enhancement reaches the maximum, and a further increase in *L* causes the field enhancement to decrease due to the decoupling of P_{2c} with P_{3c} (or the decoupling of P_{1c} with P_{2c}). Both $|E_{mean}/E_0|^2$ and $|E_{max}/E_0|^2$ at $\lambda_{P_{3c}}$ increase with *L* and show a maximum field enhancement at the coupling region but decrease with *L* when P_{3c} decouples with the LSPR-induced EOT modes. It can be seen that the *L* values of the coupled region displayed by the near-field enhancement in Figure 4d are smaller than the *L* values of the coupled region indicated by the far-field transmission spectra (Figure 4a−c). This is because there exists an energy shift between near-field and far-field peak intensities in localized plasmon systems. Upon optical excitation, the maximum near-field enhancement occurs at lower energies than the maximum of the corresponding far-field spectrum.[26] Thus, λ_0 extracted from the far-field spectra is smaller than the wavelength λ_0^N of the maximum near-field enhancements and the near-field enhancement calculated at λ_0 should be smaller than that of λ_0^N. However, the trend of near-field enhancement for the periodicity is accurate and the coupling produces a significant enhancement effect on the local electric field.

Thus, the energy exchange between the LSPR- and SPP-induced EOT modes can give rise to a higher near-field enhancement than the single SPP-induced EOT mode or the LSPR-induced EOT mode and a narrower spectral width than those of the single LSPR-induced EOT mode, but a wider spectral width than those of the single SPP-induced EOT mode. For sensing applications, the high near-field enhancement and the sharp spectral feature are highly preferred. The high local electric field enhancement can help improve the sensitivity of the spectral features due to the changes in the refractive index. A sharp peak with small FWHM facilitates the ease of the recognition of a peak shift and increases the analysis accuracy. In particular, the polarization-dependent spectra, $T(\lambda, 90°)$ and $T(\lambda, 0°)$, caused by structural anisotropy in the NRinNH can help to improve the FOM of index refractive sensing by tracking the ZCPs of the difference between these two spectra.[2] In addition, the coupling occurs in the NIR region and can be tuned to an even larger wavelength region.

https://doi.org/10.1021/acsanm.2c01962
ACS Appl. Nano Mater. XXXX, XXX, XXX−XXX

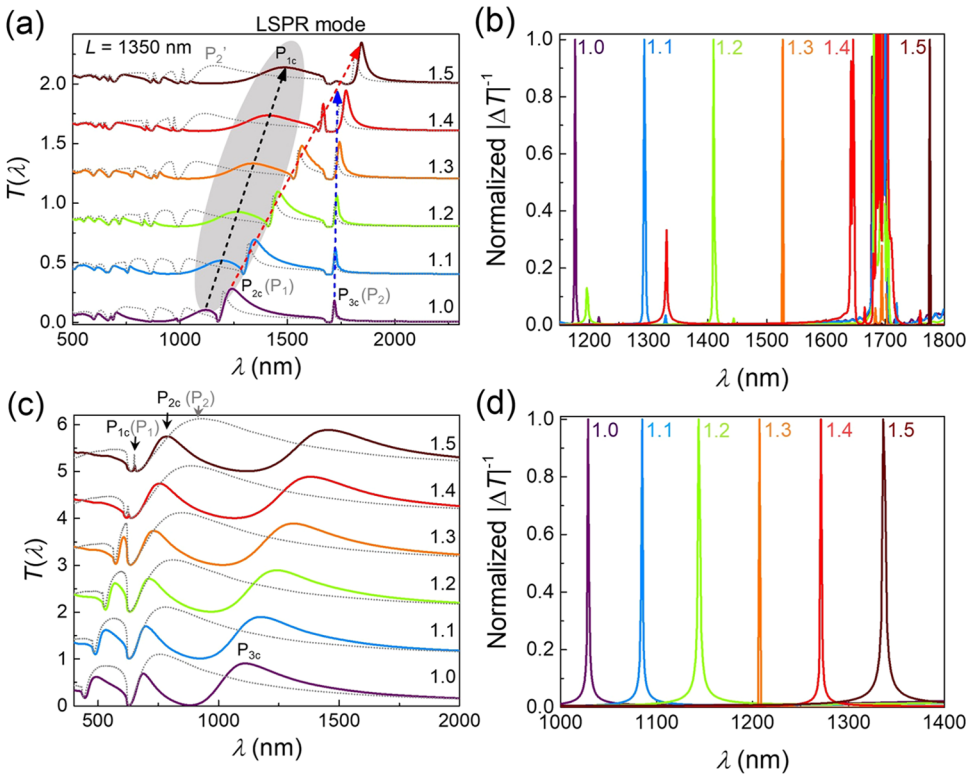

Figure 5. (a) $T(\lambda, 0°)$ (solid curves) and $T(\lambda, 90°)$ (dotted curves) spectra of the NRinNH structures with L = 1350 nm for different background indexes n. The black text is the number of peaks in $T(\lambda, 0°)$ and the gray text is the number of peaks in $T(\lambda, 90°)$. (b) Normalized $|\Delta T|^{-1}$ spectra of the intersection λ_{ZCP1} of the two most sensitive peaks (P_{2c} of $T(\lambda, 0°)$ and P_1 of $T(\lambda, 90°)$). (c) $T(\lambda, 0°)$ (solid curves) and $T(\lambda, 90°)$ (dotted curves) spectra of the NRinNH structures with L = 500 nm for different background indexes n. The black text is the number of peaks in $T(\lambda, 0°)$ and the gray text is the number of peaks in $T(\lambda, 90°)$. (d) Normalized $|\Delta T|^{-1}$ spectra of the intersection of P_{3c} of $T(\lambda, 0°)$ and P_2 of $T(\lambda, 90°)$.

The large resonance wavelength can also help to improve the RIS because of the positive relationship between RIS and the resonance wavelength λ_0.[19] Thus, as a demonstration of the improved sensing capability, the sensing performance of the NRinNH structures with coupled modes is calculated.

2.4. Refractive Index Sensitivity. Since the sensing only occurs at the Ag−air interface, we compare the shift of peaks induced by plasmon modes at this interface. The sensing performance of the NRinNH structures at the coupling region (L = 1350 nm) has been estimated by calculating the transmission spectra of the NRinNH structures submerging in different background indexes of refractions n, varying from 1.0 to 1.5. Figure 5a shows the evolution of $T(\lambda, 0°)$ (solid curves) and $T(\lambda, 90°)$ (dashed curves) of the NRinNH structure with n = 1.0−1.5. The variation of n causes all of the resonance peaks to red shift linearly and the λ_0−n slope represents the RIS. For $T(\lambda, 0°)$, the hybrid EOT peaks P_{1c} and P_{2c} of the SPP-induced EOT mode and the LSPR-induced EOT mode at the Ag−air interface red shift quickly with the increase in n since both modes generate higher near-field enhancement among all of the resonances, as shown in Figure 5a. Though the field enhancement at $\lambda_{P_{3c}}$ is at a similar value or even higher than that at $\lambda_{P_{1c}}$ and $\lambda_{P_{2c}}$, as shown in Figure 4d, the EOT peaks P_{3c} almost remain unmoved because the index of the glass remains unchanged. While for $T(\lambda, 90°)$, as discussed in Figure 2a, when the polarization is perpendicular to the long axis of the NR, the LSPR-induced EOT mode is not excited. The EOT peak P_1 induced by the resonance at the Ag−air interface shows the largest red shift. Comparing $T(\lambda, 0°)$ with $T(\lambda, 90°)$, all of the SPP-induced EOT peaks at the shorter wavelength side of the LSPR-induced EOT peak are suppressed and become narrow and opaque, while the SPP-induced EOT peaks at the longer wavelength side of the LSPR mode are enhanced and widened. Thus, $T(\lambda, 90°)$ and $T(\lambda, 0°)$ overlap at specific wavelengths, and the ZCPs of the spectra $\Delta T = T(\lambda, 0°) - T(\lambda, 90°)$ could be tracked for sensing. It should be noted that the normalization of the spectra according to $\frac{T - T_{min}}{T_{max} - T_{min}}$ (where T_{min} and T_{max} are the minimum and maximum values in the spectrum $T(\lambda)$) is necessary to obtain a better linear response and greater stability for the sensor, and the null point is more precisely visualized by plotting the quantity $|\Delta T|^{-1}$.[2] The normalized $|\Delta T|^{-1}$ spectrum (Figure 5b) shows extremely sharp peaks, with peak locations at the intersection λ_{ZCP1} of the two most sensitive peaks (P_{2c} of $T(\lambda, 0°)$ and P_1 of $T(\lambda, 90°)$). The normalized $|\Delta T|^{-1}$ spectrum of the intersection λ_{ZCP2} of P_{1c} of $T(\lambda, 0°)$ and P_2' of $T(\lambda, 90°)$ is shown in Figure S8. The FWHM values of the $|\Delta T|^{-1}$ spectrum are defined not only by the slope of the ΔT spectrum at λ_{ZCP} but also by the measurement resolution $\Delta\lambda$. In our FDTD calculation, the wavelength step used is 1.8 nm, and the normalized $|\Delta T|^{-1}$ spectrum has an FWHM of around 4.6 and 4.3 nm at λ_{ZCP2} and λ_{ZCP1}, respectively. Clearly, the change of the sharp peaks of the normalized $|\Delta T|^{-1}$ results in a much higher FOM compared to those directly using λ_0 of $T(\lambda, 0°)$ and $T(\lambda, 90°)$. The RISs of λ_{ZCP2} and λ_{ZCP1} are 622 and 1200.6 nm RIU^{-1}, which result in high FOMs of 135.2 and 279.2 RIU^{-1}, respectively. The sensing performance of the hybrid SPP mode (λ_{ZCP2}) in this structure is higher than the hybrid LSPR mode

https://doi.org/10.1021/acsanm.2c01962
ACS Appl. Nano Mater. XXXX, XXX, XXX−XXX

Table 1. RIS, FWHM, and FOM of the Peaks of $|\Delta T|^{-1}$ for the NRinNH Structure of L =1350 nm, the NR Array of L = 1350 nm, and the NRinNH Structure of L = 500 nm

structure	λ_{ZCP} (nm) at n = 1		RIS (nm RIU^{-1})	FWHM[a] (nm)	FOM (RIU^{-1})
NRinNH (L = 1350 nm)	λ_{ZCP1}	1176	1200.6	4.3	279.2
	λ_{ZCP2}	1086	622.0	4.6	135.2
NR (L = 1350 nm)			518.0	4.0	129.5
NRinNH (L = 500 nm)	1028.54		617.4	3.2	192.9

[a]The value is an average for the spectra calculated in different background indexes.

(λ_{ZCP2}) due to the large sensing area of the NH for the SPP mode. Improving the sensing area of the LSPR mode by increasing the number of the NR as the structure in ref 18 could further improve the sensitivity of the LSPR mode and get an LSPR sensor with high RIS and high FOM.

To better demonstrate the effect of coupling on different EOT modes in plasmonic sensing of the NRinNH structure, the sensing performance of the NR array of l = 200 nm and L = 1350 nm and the NH array of L = 1350 nm with the noncoupled LSPR and SPP modes is calculated (Figures S8 and S9). Due to the inverse energy change between P_{1c} and P_{2c}, the hybrid EOT peak P_{1c} of the NRinNH possesses a higher near-field enhancement, thus showing a higher sensitivity when compared with the LSPR mode of the NR of the same L and l. The RIS of the LSPR-induced EOT mode P_{1c} shown in Figure 5a is 722.6 nm RIU^{-1}, while the RIS of the LSPR mode for the NR array (λ_{NR} in Figure S9a) is only 452.1 nm RIU^{-1}. The $|\Delta T|^{-1}$ spectrum of the NR array of L = 1350 nm is shown in Figure S9b. The RIS of 518 nm RIU^{-1} and the FOM of 129.5 RIU^{-1} is obtained for the $|\Delta T|^{-1}$ spectrum of the NR array, lower than that of λ_{ZCP2} of the $|\Delta T|^{-1}$ spectrum of the NRinNH structure (622 nm RIU^{-1} and 135.2 RIU^{-1}). For the NH array, the structure does not have anisotropic property, and there is no difference between the spectra of different polarization angles. λ_0 of the transmission spectrum of the NH array is directly used to characterize the sensing performance. P_1 of the SPP mode at the Ag−air interface shows the largest red shift among all of the EOT peaks of the spectrum of the NH array (Figure S10). The highest RIS and FOM are 1204.4 nm RIU^{-1} and 30 RIU^{-1}, respectively. The RIS and FOM of the hybrid SPP mode P_{2c} of the NRinNH structure in Figure 5a (1180.3 nm RIU^{-1} and 14.6 RIU^{-1}) are a little smaller than those of the NH array (1204.4 nm RIU^{-1} and 30 RIU^{-1}) due to the increased FWHM of the hybrid mode when compared to the uncoupled SPP mode of the NH array. However, using the difference spectrum, the FOM can be increased from 30 RIU^{-1} of the NH array to 279.2 RIU^{-1} of the NRinNH structure. The sensing performance of the NRinNH structure at the noncoupled region (L = 500 nm) is also calculated and shown in Figure 5c,d. The intersection of P_{3c} of $T(\lambda, 0°)$ and P_2 of $T(\lambda, 90°)$ possesses an RIS of 617.4 nm RIU^{-1} and an FOM of 192.9 RIU^{-1}, as shown in Table 1. Clearly, the NRinNH structures of L = 1350 nm at the coupled region can obtain a high RIS and FOM simultaneously when used for plasmonic sensors.

3. CONCLUSIONS

In a summary, the separate regulation of LSPR- and SPP-induced EOT peaks can be achieved in a simple one-layer NRinNH plasmonic nanostructure. The coupling and energy exchange of SPP- and LSPR-induced EOT modes of the NRinNH structure can improve the spectral resolution and near-field enhancement of the LSPR-induced EOT mode, thus can improve the RIS of the LSPR-induced EOT peak for sensing applications. The RIS and FOM of the hybrid SPP mode of the NRinNH structure are not improved when compared to those of the NH array due to the increased FWHM when coupled with the LSPR mode. However, the hybrid modes of the NRinNH structure can be tuned to the target NIR wavelength region by the length of the NR and the periodicity of the nanostructure array, which is highly preferred for improving the RIS of the plasmonic sensor. In addition, using the polarization-dependent spectra caused by structural anisotropy, the FOM of the hybrid mode can be highly improved. A high RIS of 1200.6 nm RIU^{-1} and a high FOM of 279.2 RIU^{-1} are demonstrated for index refractive sensing applications. Meanwhile, as only the top exposed layer plays a role in the sensing process, the single-layer nanostructure design avoids the material waste of the multilayer nanostructure. The position[13] and number[18,27] of the nanorods of this NRinNH structure can be optimized according to the application scenarios and the fabrication process. As long as there is a horizontal component of the nanorods along the same direction, the separate regulation of LSPR- and SPP-induced EOT modes can be achieved by varying the NR length or the periodicity, respectively. The nanorods can also be replaced by other nanostructures capable of supporting LSPR, such as nanoparticles and nanodisks, while the nanoholes can be round or oval. It has also been shown that the preparation of large-scale complex hole structures, i.e., hole rod,[17,18] hole disk,[28,29] hole particle,[30] and hole grating,[31] can be achieved through simple processes by combing NSL and glancing angle deposition. The possible NRinNH structures by NSL are shown in Figure S11 in the SI.

■ ASSOCIATED CONTENT

Supporting Information

The Supporting Information is available free of charge at https://pubs.acs.org/doi/10.1021/acsanm.2c01962.

FDTD calculation conditions, transmission spectra of the pure NH arrays, transmission spectra of the NRinNH array with the longer rod length, electric field spectrum in the near-field showing the coupling phenomenon, coupling phenomenon tuned by the length of NR, coupled oscillator model explanation, fitted dephasing time, local-field enhancement, refractive index sensitivity, and possible NRinNH structures that can be fabricated by NSL (PDF)

■ AUTHOR INFORMATION

Corresponding Authors

Zhengjun Zhang − *Key Laboratory of Advanced Materials (MOE) and School of Materials Science and Engineering, Tsinghua University, Beijing 100084, P. R. China;*

https://doi.org/10.1021/acsanm.2c01962
ACS Appl. Nano Mater. XXXX, XXX, XXX−XXX

orcid.org/0000-0001-8727-6373; Email: zjzhang@tsinghua.edu.cn

Yiping Zhao − *Department of Physics and Astronomy, University of Georgia, Athens, Georgia 30602, United States;* orcid.org/0000-0002-3710-4159; Email: zhaoy@uga.edu

Authors

Yanfeng Wang − *Key Laboratory of Advanced Materials (MOE) and School of Materials Science and Engineering, Tsinghua University, Beijing 100084, P. R. China; Department of Physics and Astronomy, University of Georgia, Athens, Georgia 30602, United States;* orcid.org/0000-0001-7698-6230

Shen Ao − *Key Laboratory of Advanced Materials (MOE) and School of Materials Science and Engineering, Tsinghua University, Beijing 100084, P. R. China;* orcid.org/0000-0003-4365-8729

Fei Yang − *Key Laboratory of Advanced Materials (MOE) and School of Materials Science and Engineering, Tsinghua University, Beijing 100084, P. R. China*

Complete contact information is available at: https://pubs.acs.org/10.1021/acsanm.2c01962

Author Contributions

This manuscript was written through contributions of all authors. All authors have given approval to the final version of the manuscript.

Notes

The authors declare no competing financial interest.

■ ACKNOWLEDGMENTS

Y.W., S.A., and Z.Z. were supported by the Basic Science Centre Project of NSFC under Grant No. 51788104. Y.Z. was supported by the National Science Foundation under Grant No. ECCS-1808271.

■ ABBREVIATIONS

NH, nanohole
NR, nanorod
NRinNH, nanorod in nanohole
LSPR, localized surface plasmon resonance
SPP, surface plasmon polaritons
EOT, extraordinary optical transmission
NIR, near-infrared
RIS, refractive index sensitivity
RIU, refractive index (n) unit
FDTD, finite-difference time-domain
FOM, figure of merit
FWHM, full width at half-maximum
MIM, metal−insulator−metal
NSL, nanosphere lithography
COM, coupled oscillator model

■ REFERENCES

(1) Yang, J.; Sun, Q.; Ueno, K.; Shi, X.; Oshikiri, T.; Misawa, H.; Gong, Q. Manipulation of the dephasing time by strong coupling between localized and propagating surface plasmon modes. *Nat. Commun.* **2018**, *9*, No. 4858.

(2) Ai, B.; Basnet, P.; Larson, S.; Ingram, W.; Zhao, Y. Plasmonic sensor with high figure of merit based on differential polarization spectra of elliptical nanohole array. *Nanoscale* **2017**, *9*, 14710−14721.

(3) Habteyes, T. G.; Dhuey, S.; Cabrini, S.; Schuck, P. J.; Leone, S. R. Theta-shaped plasmonic nanostructures: Bringing "dark" multipole plasmon resonances into action via conductive coupling. *Nano Lett.* **2011**, *11*, 1819−1825.

(4) Kravets, V. G.; Kabashin, A. V.; Barnes, W. L.; Grigorenko, A. N. Plasmonic surface lattice resonances: A review of properties and spplications. *Chem. Rev.* **2018**, *118*, 5912−5951.

(5) Vecchi, G.; Giannini, V.; Gomez Rivas, J. Shaping the fluorescent emission by lattice resonances in plasmonic crystals of nanoantennas. *Phys. Rev. Lett.* **2009**, *102*, No. 146807.

(6) Auguié, B.; Bendaña, X. M.; Barnes, W. L.; García de Abajo, F. J. Diffractive arrays of gold nanoparticles near an interface: Critical role of the substrate. *Phys. Rev. B* **2010**, *82*, No. 155447.

(7) Chanda, D.; Shigeta, K.; Truong, T.; Lui, E.; Mihi, A.; Schulmerich, M.; Braun, P. V.; Bhargava, R.; Rogers, J. A. Coupling of plasmonic and optical cavity modes in quasi-three-dimensional plasmonic crystals. *Nat. Commun.* **2011**, *2*, No. 479.

(8) Xiang, C.-P.; Jin, Y.*Localized Surface Plasmon Resonance Modulated Double F-P Resonance Cavities to Improve the Absorption of Perovskite Solar Cells*; Recent Developments on Information and Communication Technology (ICT) Engineering, 2019; pp 9−12.

(9) Vázquez-Guardado, A.; Safaei, A.; Modak, S.; Franklin, D.; Chanda, D. Hybrid coupling mechanism in a system supporting high order diffraction, plasmonic, and cavity resonances. *Phys. Rev. Lett.* **2014**, *113*, No. 263902.

(10) Wen, L.; Sun, F.; Chen, Q. Cascading metallic gratings for broadband absorption enhancement in ultrathin plasmonic solar cells. *Appl. Phys. Lett.* **2014**, *104*, No. 151106.

(11) Yang, Z.-J.; Hu, D.-J.; Gao, F.-H.; Hou, Y.-D. Enhanced chiral response from the Fabry−Perot cavity coupled meta-surfaces. *Chin. Phys. B* **2016**, *25*, No. 084201.

(12) Zeng, P.; Cadusch, J.; Chakraborty, D.; Smith, T. A.; Roberts, A.; Sader, J. E.; Davis, T. J.; Gomez, D. E. Photoinduced electron transfer in the strong coupling regime: Waveguide-plasmon polaritons. *Nano Lett.* **2016**, *16*, 2651−2656.

(13) Wang, Y.; Zhang, Z.; Zhao, Y. The effect of nanorod position on the plasmonic properties of the complex nanorod in nanohole arrays. *J. Phys. D: Appl. Phys.* **2021**, *54*, No. 155201.

(14) Wang, Y.; Luong, H.; Zhang, Z.; Zhao, Y. Coupling between plasmonic nanohole array and nanorod array: The emerging of a new extraordinary optical transmission mode and epsilon-near-zero property. *J. Phys. D* **2020**, *53*, No. 275202.

(15) Ebbesen, T. W.; Lezec, H. J.; Ghaemi, H. F.; Thio, T.; Wolff, P. A. Extraordinary optical transmission through sub-wavelength hole arrays. *Nature* **1998**, *391*, 667−669.

(16) García de Abajo, F. J. Colloquium: Light scattering by particle and hole arrays. *Rev. Mod. Phys.* **2007**, *79*, 1267−1290.

(17) Wang, Y.; Chong, H. B.; Zhang, Z.; Zhao, Y. Large-area fabrication of complex nanohole arrays with highly tunable plasmonic properties. *ACS Appl. Mater. Interfaces* **2020**, *12*, 37435−37443.

(18) Larson, S.; Luong, H.; Song, C.; Zhao, Y. Dipole radiation-induced extraordinary optical transmission for silver nanorod-covered silver nanohole arrays. *J. Phys. Chem. C* **2019**, *123*, 5634−5641.

(19) Skehan, C.; Ai, B.; Larson, S. R.; Stone, K. M.; Dennis, W. M.; Zhao, Y. Plasmonic and SERS performances of compound nanohole arrays fabricated by shadow sphere lithography. *Nanotechnology* **2018**, *29*, No. 095301.

(20) Huang, W.-X.; Wang, Q.-J.; Yin, X.-G.; Huang, C.-P.; Huang, H.; Wang, Y.-M.; Zhu, Y.-Y. Optical resonances in a composite asymmetric plasmonic nanostructure. *J. Appl. Phys.* **2011**, *109*, No. 114310.

(21) Li, Y. Plasmonic Optics: Theory and Applications. In *Tutorial Texts in Optical Engineering*; SPIE Press: Bellingham, Washington 98227-0010 USA, 2017; Vol. *TT 110*, pp 99−129.

(22) Zhu, X.; Cao, N.; Thibeault, B. J.; Pinsky, B.; Yanik, A. A. Mechanisms of Fano-resonant biosensing: Mechanical loading of plasmonic oscillators. *Opt. Commun.* **2020**, *469*, No. 125780.

(23) Lalanne, P.; Rodier, J. C.; Hugonin, J. P. Surface plasmons of metallic surfaces perforated by nanohole arrays. *J. Opt. A: Pure Appl. Opt.* **2005**, *7*, 422−426.

(24) Lin, L.; Roberts, A. Light transmission through nanostructured metallic films: coupling between surface waves and localized resonances. *Opt. Express* **2011**, *19*, 2626−2633.

(25) Liu, H.; Sun, X.; Yao, F.; Pei, Y.; Yuan, H.; Zhao, H. Controllable coupling of localized and propagating surface plasmons to tamm plasmons. *Plasmonics* **2012**, *7*, 749−754.

(26) Zuloaga, J.; Nordlander, P. On the energy shift between near-field and far-field peak intensities in localized plasmon systems. *Nano Lett.* **2011**, *11*, 1280−1283.

(27) Song, C.; Jiang, X.; Yang, Y.; Zhang, J.; Larson, S.; Zhao, Y.; Wang, L. High-sensitive assay of nucleic acid using tetrahedral DNA probes and DNA concatamers with a surface-enhanced Raman scattering/surface plasmon eesonance dual-mode biosensor based on a silver nanorod-covered silver nanohole array. *ACS Appl. Mater. Interfaces* **2020**, *12*, 31242−31254.

(28) Ho, C.-C.; Zhao, K.; Lee, T.-Y. Quasi-3D gold nanoring cavity arrays with high-density hot-spots for SERS applications via nanosphere lithography. *Nanoscale* **2014**, *6*, 8606−8611.

(29) Yoo, D.; Mohr, D. A.; Vidal-Codina, F.; John-Herpin, A.; Jo, M.; Kim, S.; Matson, J.; Caldwell, J. D.; Jeon, H.; Nguyen, N. C.; Martin-Moreno, L.; Peraire, J.; Altug, H.; Oh, S. H. High-contrast infrared absorption spectroscopy via mass-produced coaxial zero-mode resonators with sub-10 nm gaps. *Nano Lett.* **2018**, *18*, 1930−1936.

(30) Weiler, M.; Quint, S. B.; Klenk, S.; Pacholski, C. Bottom-up fabrication of nanohole arrays loaded with gold nanoparticles: extraordinary plasmonic sensors. *Chem. Commun.* **2014**, *50*, 15419−22.

(31) Wang, Y.; Choi, I.; Zhang, K.; Yang, Y.; Ao, S.; Xue, X.; Fu, W.; Zhang, Z.; Zhao, Y. Highly conductive nanograting−nanohole structures with tunable and dual-band spectral transparency. *ACS Appl. Electron. Mater.* **2021**, *3*, 3489−3500.

https://doi.org/10.1021/acsanm.2c01962
ACS Appl. Nano Mater. XXXX, XXX, XXX−XXX